Electron-impact studies of atomic oxygen: I. Differential and integral cross sections; experiment and theory

I Kanik[1]**, P V Johnson**[1]**, M B Das**[1]**, M A Khakoo**[2] **and S S Tayal**[3]

[1] Jet Propulsion Laboratory, California Institute of Technology, 4800 Oak Grove Dr., Pasadena, CA 91109, USA
[2] Department of Physics, California State University, Fullerton, CA 92634, USA
[3] Department of Physics, Clark Atlanta University, Atlanta, GA 30314, USA

Abstract
We report both experimental and theoretical differential and integral excitation cross sections of atomic oxygen corresponding to the $2s^2 2p^4\ ^3P \rightarrow 3s\ ^3S$ (130.4 nm), $2s^2 2p^4\ ^3P \rightarrow 3d\ ^3D$ (102.7 nm), $2s^2 2p^4\ ^3P \rightarrow 3s'\ ^3D$ (98.9 nm) and $2s^2 2p^4\ ^3P \rightarrow 3s''\ ^3P$ (87.8 nm) transitions at 30, 50, and 100 eV electron-impact energies. Experimental measurements have been made in the angular range from $0°$ to $25°$ with a conventional electrostatic electron energy-loss spectrometer. The atomic O differential cross sections (DCSs) were put on an absolute scale by normalization to the O_2 DCS values of Johnson and Kanik (2001). Extrapolation of the measured results to larger angles was performed using theoretical calculations as a guide, and integral cross sections were derived. Theoretical calculations based on the R-matrix method, along with other available experimental data, have been compared with the current experimental results.

1. Introduction

Electron-impact excitation of atomic oxygen is of great interest in aeronomy and astrophysics. For example, electron-impact-induced vacuum ultraviolet (VUV) emissions of atomic oxygen are prominent features in the spectra of Earth's airglow and aurora as well as the atmospheres of other planets such as Mars and Venus. These emissions contain important diagnostic information on energy input taking place in the thermosphere (Kanik *et al* 2000). VUV emission lines of neutral atomic oxygen (the third most abundant element in normal stars) also appear in solar and stellar spectra and provide one of the primary diagnostics of physical conditions in the chromospheres and transition regions of these objects (Athay and Judge 1995). The interpretation and modelling of spectral observations requires knowledge of collision cross sections as well as radiative rate coefficients.

    Previous experimental work (both electron-impact excitation and electron-impact-induced optical emission cross section measurements) on atomic oxygen has been limited, and

Table 1. Summary of electron-impact excitation cross section measurements for atomic oxygen.

Transition	ΔE (eV)	E_0 (eV)	θ (deg)	Reference
$2s^2 2p^4\ ^3P \rightarrow 3s\ ^3S$	9.51	30, 50, 100	0–25	Present
$3d\ ^3D$	12.07	30, 50, 100	0–25	Present
$3s'\ ^3D$	12.53	30, 50, 100	0–25	Present
$3s''\ ^3P$	14.11	30, 50, 100	0–25	Present
$3s\ ^3S$	9.51	100	5–120	Doering and Vaughan (1986)
$3s\ ^3S$	9.51	16.5–200	5–120	Vaughan and Doering (1986)
$3s\ ^3S$	9.51	16.5–200	5–120	Vaughan and Doering (1987)
$3s'\ ^3D$	12.51	20–200	5–120	Vaughan and Doering (1987)
$3s''\ ^3P$	14.11	30–200	5–120	Vaughan and Doering (1988)
$2s2p^5\ ^3P$	15.66	30–200	5–120	Vaughan and Doering (1988)
$4d'\ ^3P$	16.11	30–200	5–120	Vaughan and Doering (1988)
$nd\ ^3D\ (n = 3\text{--}7)$	12.07–13.34	30–100	5–120	Vaughan and Doering (1988)
$3p\ ^3P$	10.99	30	2–130	Gulcicek and Doering (1987)
$3p\ ^5P$	10.76	30	25–130	Gulcicek and Doering (1987)
$3p\ ^3P$	10.99	13.9–100	0–135	Gulcicek *et al* (1988)
$3p\ ^5P$	10.76	13.9–100	0–135	Gulcicek *et al* (1988)
$2p^4\ ^1D$	1.97	4–30	10–130	Doering and Gulcicek (1989a)
$2p^4\ ^1S$	4.19	7–30	20–135	Doering and Gulcicek (1989a)
$3s\ ^5S$	9.14	13.9–30	20–135	Doering and Gulcicek (1989b)
$2p^4\ ^1D$	1.97	3.5–30	80–134	Doering (1992)
$3s\ ^3S$	9.51	13.4–38.6	10–130	Doering and Yang (2001)
$2p^4\ ^1D$	1.97	7–30	30–150	Shyn and Sharp (1986)
$2p^4\ ^1S$	4.19	10–30	30–150	Shyn *et al* (1986)

large discrepancies exist among the published data as demonstrated in the comparison of electron-impact studies provided by Wang and McConkey (1992). This is largely due to the experimental difficulties associated with generating and handling atomic oxygen for laboratory measurements. DSCs and integral cross sections (ICSs) for excitation of various levels in atomic oxygen have been studied using energy-loss spectroscopy by Doering and co-workers (Doering and Vaughan 1986, Vaughan and Doering 1986–1988, Gulcicek and Doering 1987, 1988, Gulcicek *et al* 1988, Doering and Gulcicek 1989a, b, Doering and Yang 2001). Shyn and co-workers measured electron-impact differential excitation cross sections of atomic oxygen for the $2s^2 2p^4\ ^3P \rightarrow 2s^2 2p^4\ ^1D$ and $2s^2 2p^4\ ^3P \rightarrow 2s^2 2p^4\ ^1S$ transitions by employing electron energy-loss spectroscopy (Shyn and Sharp 1986, Shyn *et al* 1986). Emission cross sections for atomic O were measured by Stone and Zipf (1974), Zipf *et al* (1979), Zipf and Kao (1983, 1986), Zipf and Erdman (1985), Zipf (1986), Erdman and Zipf (1987), Wang and McConkey (1992), and most recently by Noren *et al* (2001).

On the theoretical side, a large number of calculations of electron-impact differential excitation and integral excitation cross sections for atomic oxygen have been reported over the past 25 years (Rountree and Henry 1972, Julienne and Davis 1976, Smith 1976, Rountree 1977). More recently, Tayal and Henry (1988–1990) calculated electron-impact differential excitation cross sections and integral excitation cross sections using multi-state close-coupling theory and compared their results with available data. Serious discrepancies between the theoretical and experimental results exist. Often, various theoretical calculations are not consistent with each other in magnitude and/or shape of the excitation function.

A comprehensive review on cross sections for collisions of electrons with atomic oxygen was given by Itikawa and Ichimura (1990) and more recently by Zecca *et al* (1996). Tables 1

Table 2. Summary of electron-impact-induced emission cross section measurements for atomic oxygen.

Transition[a]	ΔE (eV)	E_0 (eV)	Ref.
$2s^2 2p^4\ ^3P \rightarrow 3s\ ^3S$ (130.4)	9.51	Tr–100[b]	Wang and McConkey (1992)
$3d\ ^3D$ (102.7)	12.07	Tr–100	Wang and McConkey (1992)
$3s'\ ^3D$ (98.9)	12.53	Tr–100	Wang and McConkey (1992)
$3s''\ ^3P$ (87.8)	14.11	Tr–100	Wang and McConkey (1992)
$3s\ ^3S$ (130.4)	9.51	Tr–1000	Noren *et al* (2001)
$3s\ ^3S$ (130.4)	9.51	Tr–300	Stone and Zipf (1974)
$3s\ ^5S$ (135.6)	9.14	Tr–300	Stone and Zipf (1974)
$3s\ ^3S$ (130.4)	9.51	Tr–300	Zipf and Erdman (1985)
$3s\ ^5S$ (135.6)	9.14	Tr–300	Zipf and Erdman (1985)
$3d\ ^3D$ (102.7)	12.07	Tr–300	Zipf and Erdman (1985)
$3s'\ ^3D$ (98.9)	12.53	Tr–300	Zipf and Erdman (1985)
$3s''\ ^3P$ (87.8)	14.11	Tr–300	Zipf and Kao (1986)

[a] The wavelength is given in parentheses (nm).
[b] Tr stands for threshold.

and 2 summarize electron-impact excitation cross section measurements for atomic O.

We felt that additional effort for detailed experimental and theoretical studies of electron-impact excitation cross sections for atomic oxygen was needed to clear the discrepancy that currently exists between the available data sets. Specifically, we felt that new experimental and theoretical differential cross section (DCS) determinations based on improved normalization procedures and new theoretical methods, respectively, were warranted. In this paper, we report both experimental and theoretical differential and integral excitation cross sections of atomic oxygen at impact energies of 30, 50, and 100 eV corresponding to the $2s^2 2p^4\ ^3P \rightarrow 3s\ ^3S$ (130.4 nm), $2s^2 2p^4\ ^3P \rightarrow 3d\ ^3D$ (102.7 nm), $2s^2 2p^4\ ^3P \rightarrow 3s'\ ^3D$ (98.9 nm) and $2s^2 2p^4\ ^3P \rightarrow 3s''\ ^3P$ (87.8 nm) transitions.

2. Experimental procedures

Both the electron-impact spectrometer and the experimental techniques used for the DCS measurements have been described previously by Trajmar and Register (1984) and more recently by Trajmar and Kanik (1995). A schematic of the spectrometer is given in figure 1. The electron gun consists of a heated rhenium filament (which behaves well in the oxygen environment), electrostatic cylindrical optics and hemispherical energy selectors. The gun forms a well-collimated, nearly mono-energetic beam (∼0.050 eV energy resolution FWHM: full width at half maximum) with the desired impact energy, E_0. This beam crosses the target atomic (molecular) beam at 90°. The target beam (atomic O) is produced by an extended air-cooled microwave cavity through the dissociation of a gas mixture which contains 95% O_2 and 5% N_2. The use of N_2 as a buffer gas enhances the performance of the source in terms of the dissociation fraction. A similar source was described originally by Murphy and Brophy (1979) and later by Doering and co-workers (Doering *et al* 1985a, b, Gulcicek and Doering 1988). A quartz tube is used to transport the gas mixture through the microwave cavity where dissociation of oxygen molecules takes place (typically 20–35% under the present operating conditions). The resulting mixture of atomic and molecular oxygen is then transported by the same tube to the interaction region. In order to achieve a stable dissociation, the quartz tube is cleaned using ortho-phosphoric acid. The exit region of the tube is coated with Teflon in order to minimize recombination of the oxygen atoms during transport. A Teflon plug with a 2 mm
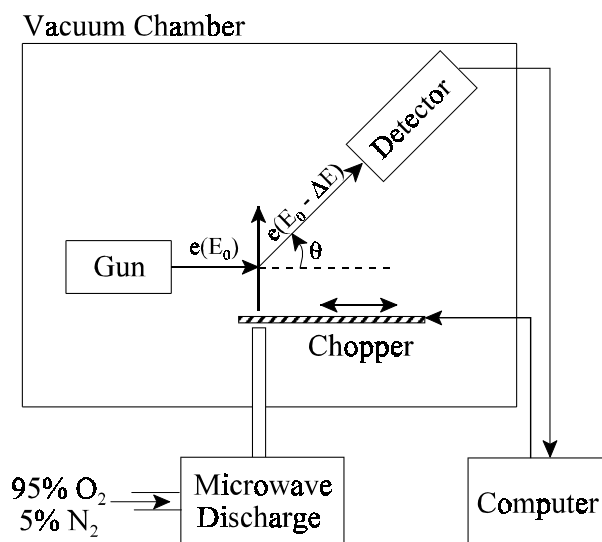
Vacuum Chamber

Figure 1. A schematic representation of the experimental arrangement.

diameter hole is placed at the end of the quartz tube which allows the target gas to effuse into the interaction region with minimal recombination of the atomic oxygen component. The Teflon plug is covered with an electrically-grounded titanium piece to maintain an electric-field-free interaction region. The target beam, based on our preliminary measurements, consisted of $O_2(^3\Sigma_g^-)$, $O(^3P)$, a negligible amount (less than a few per cent) of $O_2(a\ ^1\Delta)$, and the N_2 buffer gas. It should be noted that we were not able to detect any evidence of neutral atomic nitrogen in the target beam. We, therefore, conclude that any atomic N, produced in the source, recombined to form N_2 before reaching the interaction region. However, both the 108.5 nm N^+ (James *et al* 1990) and 95.8 nm N_2 (Ajello *et al* 1989) features were observed. Both were easily separated from the atomic O features under investigation.

During the measurements, the oxygen source was adjusted to give a roughly 1:1 correspondence between the intensities of the 130.4 nm (9.51 eV energy loss) feature in atomic O and the longest band (LB; 9.98 eV energy loss) in O_2. This level of dissociation was maintained to ensure good statistics in both the atomic O features that we wished to measure and the O_2 features which were employed in the subsequent normalization. Throughout the course of the measurements, the stability of the O_2 dissociation fraction was periodically confirmed by monitoring the relative 16 (O) and 32 (O_2) amu signals with a quadrupole mass spectrometer placed downstream of the discharge tube exit nozzle.

The electrons scattered by this mixed beam at a given angle, θ, were collected over a small solid angle ($\sim 10^{-3}$ sr) and analysed for their residual energy. Like the electron gun, the detector consists of cylindrical electron optics and hemispherical energy selectors. Energy-loss spectra are obtained at fixed E_0 and θ by recording the scattering intensities as a function of the energy lost by the incident electron. Proper signal to noise conditions are achieved by using pulse counting and multi-channel scaling techniques. These energy-loss spectra give us the information needed for deriving various excitation cross sections. The location of a feature (in energy-loss) identifies the associated excited atomic/molecular state while the intensity (area under the feature) is proportional to the corresponding cross section.

Energy-loss spectra for atomic oxygen covering the 6.5–16.5 eV energy-loss region were

obtained at fixed impact energies of 30, 50, and 100 eV over the angular range of 0–25° with about 50 meV resolution (FWHM). This proved sufficient to resolve the various atomic O and O_2 features found in the measured spectra. As a note, the DCSs of the studied transitions dropped-off by up to four orders of magnitude with increasing scattering angle between 0° and 90°. Beyond an angle of 25°, the scattering signal intensity became comparable to the background signal and was found to be unreliable. Theoretical calculations were relied upon beyond angles of 25° for the extrapolation needed to obtain integral cross sections as explained in the next section.

At every combination of impact energy and scattering angle, energy-loss spectra were concurrently obtained with the target beam on and off using a molybdenum chopper (i.e. alternating between the two) and are referred to as ON and BKG spectra, respectively. When the target beam was turned off, target gas, with the discharge on, was admitted into the vacuum chamber to maintain a consistent background pressure of O_2 and N_2 without disrupting the operation of the source (all atomic O having recombined). Therefore, the 'ON' spectra contained signals due to scattering from the target beam constituents (O, O_2, N^+, and N_2) as well as from the background (O_2 and N_2 molecules and various surfaces) while the BKG spectra contained only those due to the background. The BKG spectra were used to account for background signals present in their associated ON spectra. Since both the ON and BKG spectra were taken under identical experimental conditions, subtraction of the BKG spectra from their parent ON spectra left spectra free of all background signals due to scattering from residual gases, surfaces in the vacuum chamber, as well as any electronic noise that may have been present (i.e. leaving clean target beam spectra: $O + O_2 + N^+ + N_2$).

Target beam on and off spectra were also taken with the discharge turned off. These discharge off spectra are referred to as OFF and BKG spectra, respectively. The BKG spectra were subtracted from their parent OFF spectra in direct analogy to the discharge ON spectra of the preceding paragraph. This procedure produced background-free, OFF spectra ($O_2 + N_2$). By comparing O_2 feature intensities in the ON spectra ($O + O_2 + N^+ + N_2$) and the OFF spectra ($O_2 + N_2$), the molecular dissociation fraction could be determined.

A typical example of each type of electron energy-loss spectrum (i.e. ON, OFF, and BKG) is shown in figure 2. Figure 2(*a*) shows an ON spectrum (beam on, discharge on) which contains scattering contributions from the target beam ($O + O_2 + N^+ + N_2$), as well as background. Figure 2(*b*) shows an example of a BKG spectrum (beam off, discharge on). It should be noted that the BKG spectra taken with the discharge off are essentially the same as those taken with the discharge on, and so an example is not shown in figure 2. An example of an OFF spectrum (beam on, discharge off) is given in figure 2(*c*). The presented examples were taken at an impact energy of 100 eV with a scattering angle of 10°.

3. Data analysis

The measured energy-loss spectra at 30, 50, and 100 eV were used to obtain angular distributions (relative DCSs) for transitions in atomic O and O_2 at each measured angle between 0° and 25° as follows. After removing any background signals by appropriate subtractions, as described previously, signals lying below the various O and O_2 features coming from the high-energy tail of the Shumann–Runge bands ($\lesssim 9.5$ eV) as well as the ionization continuum ($\gtrsim 12$ eV) in O_2 (see figure 2) and the 95.8 nm N_2 feature were removed. This was accomplished by fitting a straight line to the regions surrounding a given feature and subtracting the result from the feature plus O_2 and N_2 signals where appropriate.

As alluded to earlier, absolute atomic O DCSs at a given energy and angle were obtained by scaling their corresponding intensities relative to intensities of O_2 features present in the
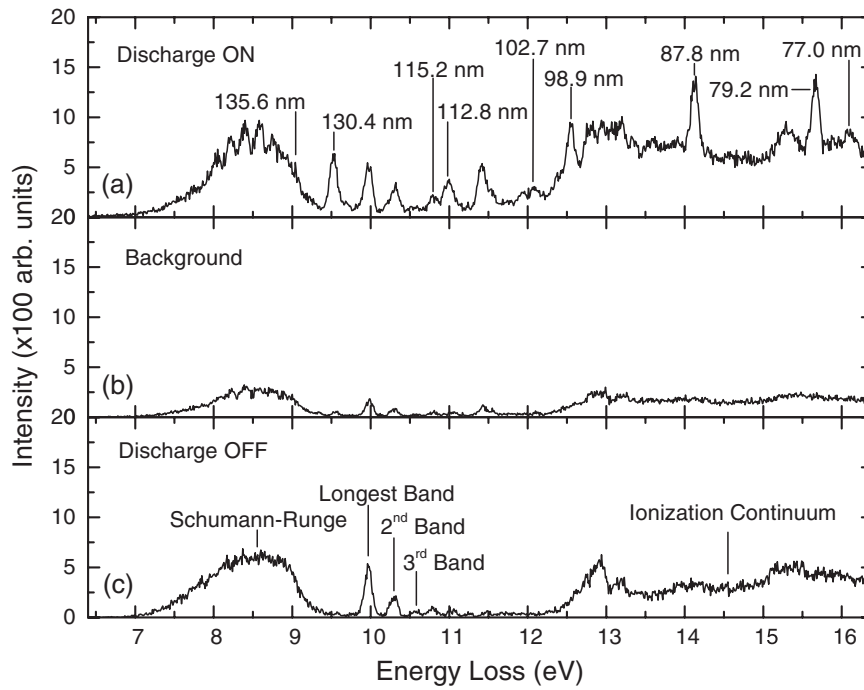
Figure 2. Examples of (*a*) ON (beam on, discharge on), (*b*) BKG (beam off, discharge on), and (*c*) OFF (beam on, discharge off) spectra taken at 100 eV impact energy and 10° scattering angle. Atomic O features are indicated in (*a*) while O_2 features are indicated in (*c*). In addition, the 108.5 N^+ ($\Delta E \simeq 11.4$ eV) and 95.8 nm N_2 ($\Delta E \simeq 12.9$ eV) features can easily be seen in (*a*) and (*c*), respectively. The absence of the 108.5 nm line in (*c*) indicates that the N^+ observed in (*a*), and to a lesser degree (*b*), originated through dissociation of N_2 in the microwave discharge source.

spectra. In order to take advantage of the best statistics possible, the intensities of each examined atomic O feature in a given spectrum, I_x^{on} (where '*x*' denotes a particular feature), were determined relative to the corresponding summed intensities of the LB, second band (2B), and third band (3B) features in O_2, $I_\Sigma^{on} = I_{LB}^{on} + I_{2B}^{on} + I_{3B}^{on}$, which were clearly resolved from any atomic O features in the measured spectra. This can be expressed in the relation

$$\frac{I_x^{on}}{I_\Sigma^{on}} = \frac{K_x^{on} n_O^{on} DCS_x}{K_\Sigma^{on} n_{O_2}^{on} DCS_\Sigma} \tag{1}$$

in terms of the number densities, n, of O and O_2, the absolute DCSs of atomic feature x, DCS_x, and the summed O_2 cross sections, $DCS_\Sigma = DCS_{LB} + DCS_{2B} + DCS_{3B}$. The K values in equation (1) include multiplicative factors such as effective scattering volume, detector efficiency, gun current, and the number of scans taken across the energy-loss range. Since the O and O_2 feature intensities in question are found in the same spectrum, the ratio of K values in this expression is equal to unity.

The remaining unknown in equation (1), namely the ratio of O to O_2 number densities, is related to the dissociation fraction, D. By assuming thermal equilibrium, along with a Boltzmann velocity distribution, within the O/O_2 beam, one can show (see appendix), by means of a straightforward rate flow analysis, that the O to O_2 number density ratio is given

by $2^{1/2}D/(1-D)$. Therefore, the absolute atomic DCS of feature x is given by

$$\mathrm{DCS}_x = \frac{(1-D)}{\sqrt{2}D} \frac{I_x^{\mathrm{on}}}{I_\Sigma^{\mathrm{on}}} \mathrm{DCS}_\Sigma. \tag{2}$$

It should be noted that in deriving equation (2), it was assumed that two neutral ground-state O atoms were produced for every O_2 molecule that remained dissociated at the interaction region. It is, however, conceivable that other dissociation products such as oxygen ions and/or metastable oxygen atoms (O I (^{1}D) and O I (^{1}S) at 2.0 and 4.2 eV above the ground state, respectively) were formed. Doering *et al* (1985a), who used a similar oxygen source, found no evidence of such products in their gas beam and gave an upper limit of 1.5% for the fraction of the total atomic O population produced in the metastable O I (^{1}D) state. Current investigations into the gas beam composition resulted in identical conclusions. Therefore, the aforementioned assumption was deemed to be valid.

The dissociation fraction at the interaction region, D, was determined by comparing the integrated intensities of the LB in the ON and OFF spectra taken at a given angle and energy, $I_{\mathrm{LB}}^{\mathrm{on/off}}$. The dissociation fraction, which gives the fraction of molecules that are dissociated in the source, and remain dissociated at the interaction region, can be expressed in terms of the ratio of O_2 molecules present in the ON spectra, $n_{O_2}^{\mathrm{on}}$, and the number of O_2 molecules in the OFF spectra, $n_{O_2}^{\mathrm{off}}$, which in turn can be expressed in terms of the measured LB integrated intensities in the ON and OFF spectra as

$$(1-D) = \frac{n_{O_2}^{\mathrm{on}}}{n_{O_2}^{\mathrm{off}}} = \frac{K^{\mathrm{off}}}{K^{\mathrm{on}}} \frac{I_{\mathrm{LB}}^{\mathrm{on}}}{I_{\mathrm{LB}}^{\mathrm{off}}}, \tag{3}$$

where the K values again represent multiplicative factors such as effective scattering volume, detector efficiency, gun current, and the number of scans taken across the examined energy-loss range. In the current measurements, ON and OFF spectra, at a given angle and impact energy, were taken under the same experimental conditions (i.e. gun current, source pressure, etc), and so the $K^{\mathrm{on}}/K^{\mathrm{off}}$ ratio reduces to the ratio of the number of scans taken with discharge ON to the number taken with discharge OFF.

Following this procedure, the dissociation fraction was determined to be 0.310 ± 0.027 in all measured 30 and 50 eV spectra, while the dissociation fraction was found to be 0.216 ± 0.027 in the 100 eV spectra. As mentioned in the previous section, the operation of the oxygen source was engineered to provide a consistent dissociation fraction throughout all of the measurements at a given energy. This was confirmed by the analysis described above and by the mass spectrometer employed to monitor the stability of the source.

Using the analytical approach outlined above (equations (1)–(3)), the measured atomic O relative DCSs were put on an absolute scale by normalizing to the absolute O_2 DCS values of Johnson and Kanik (2001).

ICSs were obtained by extrapolating the DCSs to 180° and then integrating them over all angles. For this procedure, we relied on the general trend of the data along with the theoretical predictions of the R-matrix theory as a guide. Extrapolated data were chosen based on the aforementioned criteria in 10° intervals. A cubic spline interpolation method was then employed which enabled numerical integration of the DCSs.

As will be seen in section 5, the investigated DCSs exhibit a change of three to four orders of magnitude from 0° to beyond the measured 25° angular range. Therefore, if the 0° data could be measured in 10 min (taken as an example), the high-angle values would require acquisition times of 7–70 d in order to obtain data of similar statistical reliability. Adequate stability of experimental conditions (electron beam current, dissociation fraction, etc) over these timescales is unrealistic, and, therefore, theory was taken to be more reliable

than available experimental values at high angles. It was for this reason that theory was used to guide the DCS extrapolations.

4. Theoretical approach

Theoretical calculations for differential and integral excitation cross sections of atomic oxygen by electron impact were carried out using the R-matrix approach (Berrington *et al* 1995) with multi-configuration-interaction target wavefunctions. The scattering wavefunction

$$\Psi_k = A\sum_{ij}c_{ijk}\overline{\Phi}(1, 2, \ldots, 8, s_9, \sigma_9)\frac{1}{r_9}u_{ij}(r_9) + \sum_j d_{jk}\varphi_j(1, 2, \ldots, 9) \qquad (4)$$

for each LS symmetry is expanded in the inner region ($r \leqslant a$, where a is the R-matrix radius) in the R-matrix basis (Berrington *et al* 1995) where A is the antisymmetrization operator. The functions $\overline{\Phi}$ are formed by coupling the multi-configurational functions of the target bound states with the spin (s_9) and orbital (σ_9) angular momenta of the scattered electron. u_{ij} are the numerical basis functions for the scattered electron where r_9 gives the position of the scattered electron. The functions φ_j are formed from the atomic orbitals and are included to ensure completeness of the scattering wavefunction expansion and to allow for short-range correlation. The c_{ijk} and d_{jk} are expansion coefficients that are determined by diagonalizing the ($N + 1$)-electron Hamiltonian. We included 22 LS target states ($2p^4\ ^3P$, $2p^33s\ ^5S^o$, $^3S^o$, $2p^33p\ ^5P$, ^3P, $2p^34s\ ^5S^o$, $^3S^o$, $2p^33d\ ^5D^o$, $^3D^o$, $2p^34p\ ^5P$, ^3P, $2p^33s'\ ^3D^o$, $2p^35s\ ^5S^o$, $^3S^o$, $2p^34d\ ^5D^o$, $^3D^o$, $2p^34f\ ^5F$, $2p^33s''\ ^3P^o$, $2p^33d'\ ^3P^o$, $2p^34d'\ ^3P^o$, and $2s2p^5\ ^3P^o$) in the close-coupling expansion. The multi-configurational functions of the target states are constructed with a common set of radial functions chosen to give good representation of the excitation energies of the 22 LS states and oscillator strengths of the dipole-allowed transitions among these states. Eleven orthogonal one-electron orbitals 1s, 2s, 2p, 3s, 3p, 3d, 4s, 4p, 4d, 4f, and 5s are used in our calculation. We started with the atomic oxygen $2p^4\ ^3P$ Hartree–Fock orbitals 1s, 2s, and 2p given by Clementi and Roetti (1974) and obtained other orbitals with the computer code CIV3 (Hibbert 1975) by optimizing the energies of the states. The radial part of each orbital is expressed in analytical form as a sum of Slater-type orbitals. The exponents and coefficients are determined variationally. The orbitals 3s, 3p, 3d, 4s, 4p, 4d, 4f, and 5s are all chosen of spectroscopic type and are optimized on the excited states $2p^33s$, $2p^33p$, $2p^33d$, $2p^34s$, $2p^34p$, $2p^34d$, $2p^34f$, and $2p^35s$, respectively. The 22 LS states are represented by 241 configurations. An R-matrix radius of $a = 61.6\ a_0$ (where a_0 is the Bohr radius) is chosen to accommodate all 11 orbitals. We included 72 Lagrange-orthogonalized continuum orbitals in each channel, which gave good convergence for energies up to 100 eV. In order to match the calculated thresholds to the experiment, we adjusted the energies of the target states to reproduce the observed values in the scattering calculation. The diagonal elements of the inner-region Hamiltonian matrix are also adjusted before diagonalization. We carried out R-matrix calculations for partial waves with $L = 0$–80. For each LS symmetry, the R-matrix was calculated at the boundary and matched to solutions in the outer region to obtain the appropriate K-matrix, from which the differential and integral cross sections were then obtained.

5. Results

The experimentally and theoretically determined DCSs at 30, 50, and 100 eV impact energies are plotted in figures 3–5, respectively, along with the results of Vaughan and Doering (1987, 1988). The measured data are also tabulated in tables 3–6. These tables include recommended

Table 3. $2s^2 2p^4\ ^3P \rightarrow 3s\ ^3S$ (130.4 nm, $\Delta E_0 = 9.51$ eV).

	DCS ($\times 10^{-18}$ cm^2 sr^{-1})		
θ (deg)	$E_0 = 30$ eV	$E_0 = 50$ eV	$E_0 = 100$ eV
0	34.75 ± 9.38	72.50 ± 19.58	273.36 ± 62.87
5	24.83 ± 6.70	46.64 ± 12.59	57.49 ± 13.22
10	23.35 ± 6.30	22.87 ± 6.18	12.66 ± 2.91
15	9.84 ± 2.66	7.77 ± 2.10	2.21 ± 0.51
20	3.25 ± 0.88	2.05 ± 0.55	1.31 ± 0.30
25	1.12 ± 0.30	0.79 ± 0.21	0.24 ± 0.05
30	0.6	0.5	0.12
40	0.3	0.23	0.07
50	0.23	0.13	0.03
60	0.21	0.09	0.016
70	0.19	0.06	0.014
80	0.17	0.04	0.012
90	0.13	0.025	0.01
100	0.09	0.013	0.012
110	0.07	0.013	0.017
120	0.08	0.029	0.027
130	0.15	0.06	0.035
140	0.28	0.1	0.045
150	0.45	0.15	0.055
160	0.6	0.25	0.06
170	0.7	0.35	0.065
180	0.82	0.45	0.07
ICS[a] (expt)	8.3 ± 2.4	7.4 ± 2.1	5.9 ± 1.5
ICS (VD[b])	8.69 ± 2.8	7.81 ± 1.4	6.30 ± 1.0
ICS (thry)	11.01	10.19	7.81

[a] ICS in units of 10^{-18} cm^2.
[b] Vaughan and Doering (1987).

absolute DCS values beyond the measured angular range. As discussed previously, these values were chosen based on the general trend of the measured data, along with the behaviour of the *R*-matrix calculations, and were used to generate ICSs which are also listed, along with the *R*-matrix ICS results, in tables 3–6. In addition, we have included the ICS results of Vaughan and Doering (1987, 1988) for convenient comparison. All experimentally determined data are tabulated along with their associated experimental uncertainties while recommended values are shown without any errors quoted.

It should be noted that the published works of Vaughan and Doering (1987, 1988) did not include error estimates for the DCS values presented. However, uncertainties were quoted for the ICS values which ranged between 16 and 37% for the presently investigated transitions and energies. In the absence of DCS uncertainties, the quoted ICS uncertainties were applied to the corresponding DCSs and are included in the plots.

The error bars quoted for the present DCS measurements include statistical uncertainties, uncertainties in the background determination, as well as uncertainties in the normalization procedure. Statistical uncertainties in the DCS measurements were estimated to be 15% in the 30 and 50 eV data sets and 10% in the 100 eV data set. Up to as many as ten ON and OFF spectra were taken at each energy and angle and combined to form the final ON and OFF spectra. The high degree of consistency between these independently acquired spectra was taken as a sign of statistical quality.
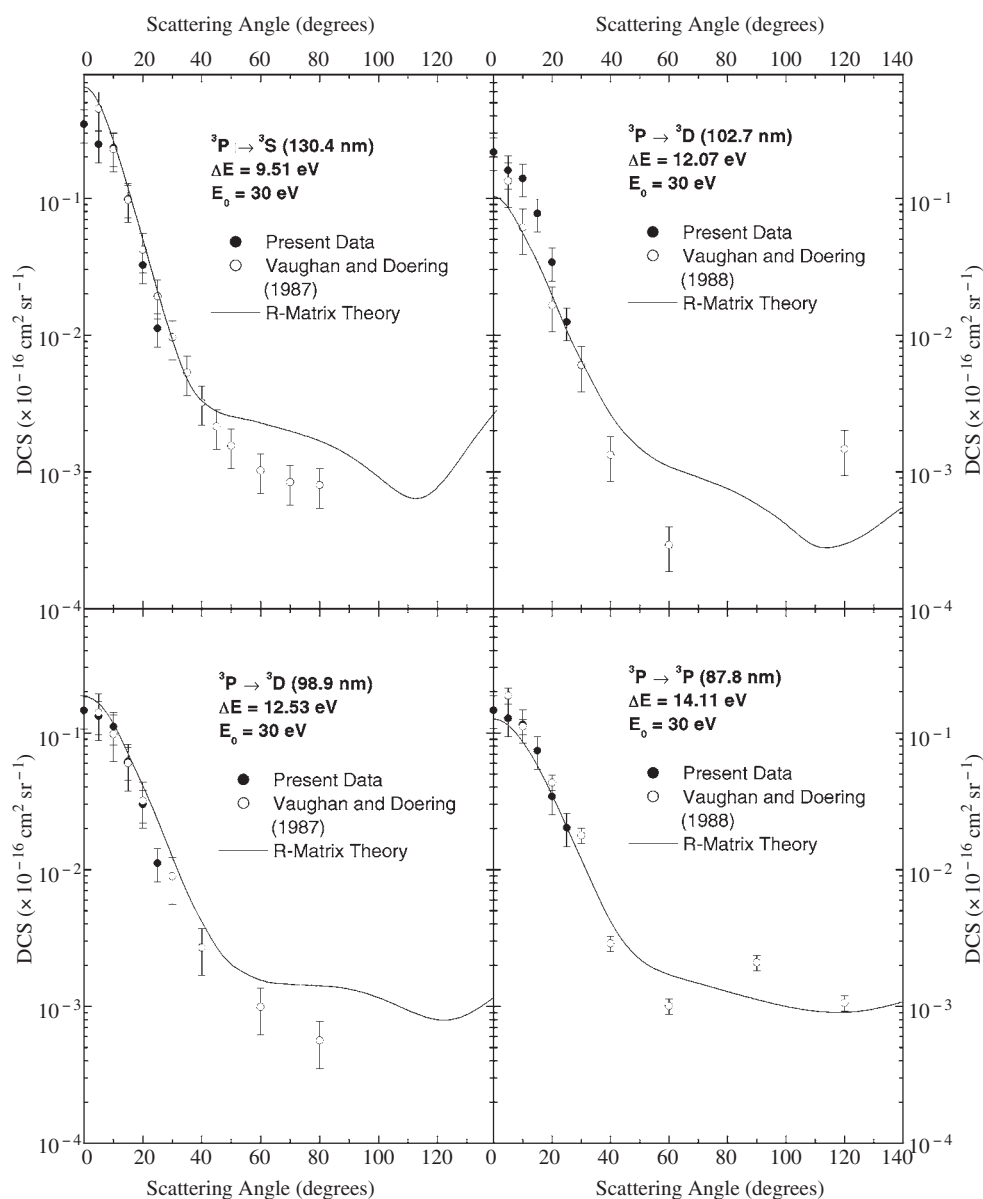
Figure 3. Experimental and theoretical DCSs at 30 eV impact energy are shown along with the results of Vaughan and Doering (1987, 1988) for the $2s^2 2p^4\ ^3P \rightarrow 3s\ ^3S$, $3d\ ^3D$, $3s'\ ^3D$, and $3s'\ ^3P$ transitions at 130.4 (9.51), 102.7 (12.07), 98.9 (12.53), and 87.8 (14.11) nm (eV), respectively.

Background determination and subtraction, including separation of signals from the Schumann–Runge bands and the ionization continuum of O_2, was performed to within an estimated 5% accuracy. The accuracy of this procedure was limited by the uncertainties in the background measurements along with the errors associated with representing the underlying O_2 (and 95.8 nm N_2) signals with a linear fit.
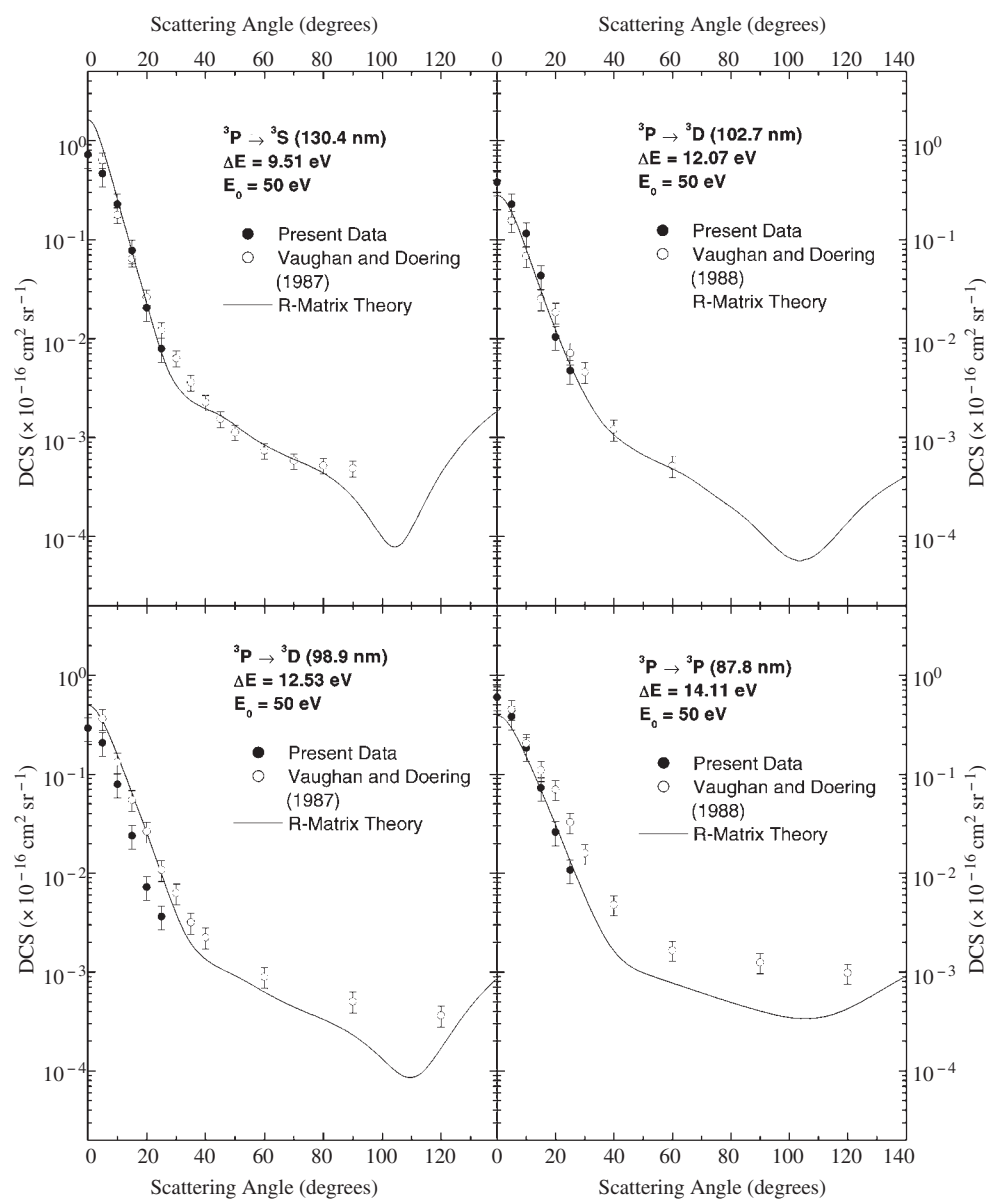
Figure 4. Experimental and theoretical DCSs at 50 eV impact energy are shown along with the results of Vaughan and Doering (1987, 1988) for the $2s^2 2p^4 \, ^3P \rightarrow 3s \, ^3S$, $3d \, ^3D$, $3s' \, ^3D$, and $3s'' \, ^3P$ transitions at 130.4 (9.51), 102.7 (12.07), 98.9 (12.53), and 87.8 (14.11) nm (eV), respectively.

Uncertainty in the normalization of the DCSs arose from two sources. First was the uncertainty in the summed DCS values for O_2 of Johnson and Kanik (2001) which were used as normalization standards. The errors in these numbers are quoted as 18% at 30 and 50 eV and 13% at 100 eV. Uncertainty in the normalization was also introduced by the determination of the dissociation fraction. The error assigned (universally) to the dissociation fraction was taken as the worst case standard deviation observed among spectra taken at the same impact
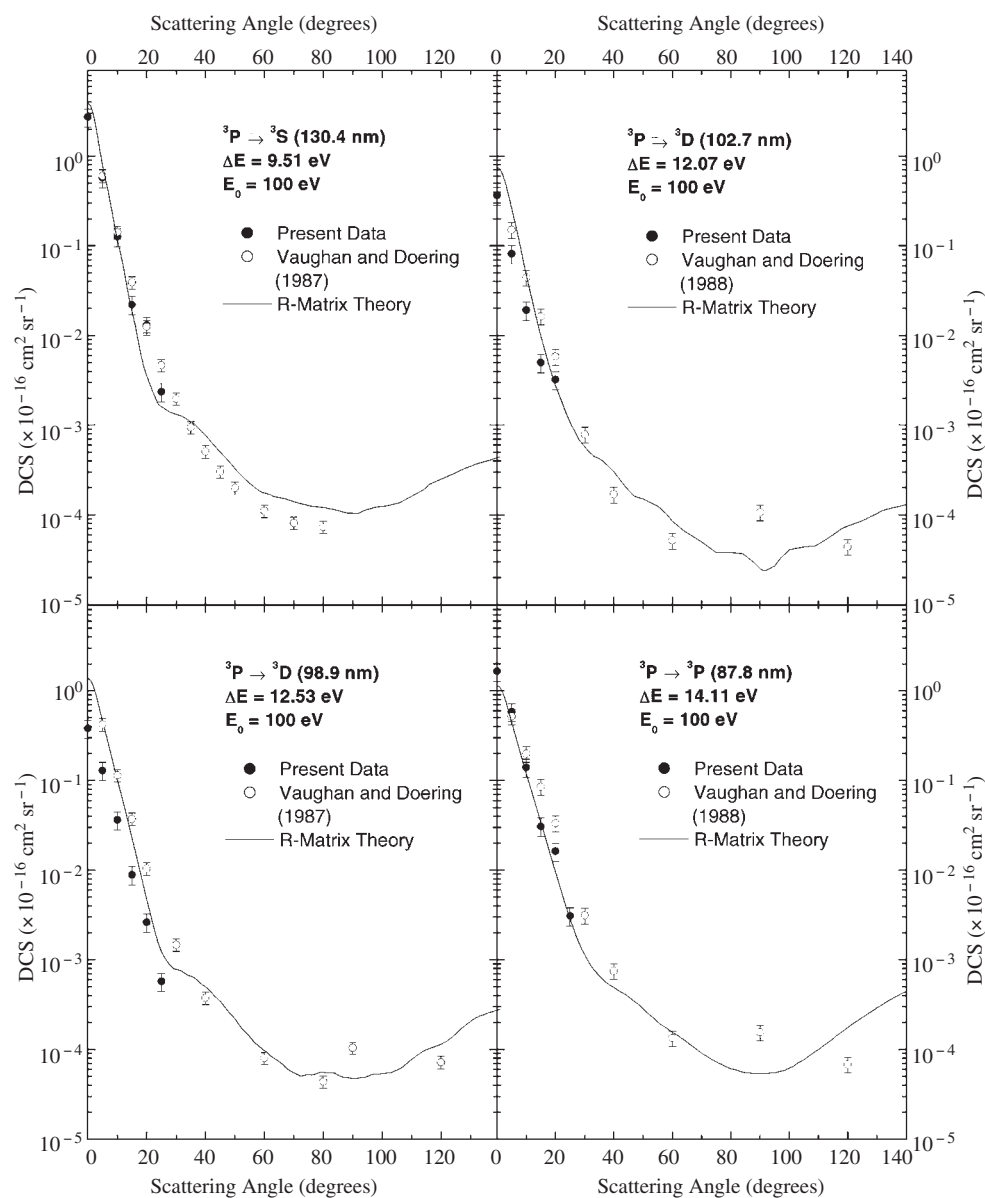
Figure 5. Experimental and theoretical DCSs at 100 eV impact energy are shown along with the results of Vaughan and Doering (1987, 1988) for the $2s^2 2p^4 \, ^3P \rightarrow 3s \, ^3S$, $3d \, ^3D$, $3s' \, ^3D$, and $3s'' \, ^3P$ transitions at 130.4 (9.51), 102.7 (12.07), 98.9 (12.53), and 87.8 (14.11) nm (eV), respectively.

energy. Although the dissociation fraction was determined to within ± 0.027, this translated into an uncertainty in the $2^{-1/2}D^{-1}(1-D)$ factor found in equation (2) of 13% at 30 and 50 eV and 16% at 100 eV.

The uncertainties mentioned in the preceding paragraphs were combined to produce the error limits assigned to the DCS data. This yielded error limits of 27% at 30 and 50 eV and 23% at 100 eV.

Table 4. $2s^2 2p^4\ ^3P \rightarrow 3d\ ^3D$ (102.7 nm, $\Delta E_0 = 12.07$ eV).

	DCS ($\times 10^{-18}$ cm^2 sr^{-1})		
θ (deg)	$E_0 = 30$ eV	$E_0 = 50$ eV	$E_0 = 100$ eV
0	21.74 ± 5.87	38.04 ± 10.27	36.71 ± 8.44
5	15.98 ± 4.32	22.85 ± 6.17	8.15 ± 1.88
10	13.97 ± 3.77	11.54 ± 3.12	1.92 ± 0.44
15	7.74 ± 2.09	4.32 ± 1.17	0.50 ± 0.11
20	3.41 ± 0.92	1.04 ± 0.28	0.32 ± 0.07
25	1.25 ± 0.34	0.48 ± 0.13	0.145
30	0.6	0.25	0.09
40	0.3	0.1	0.03
50	0.15	0.07	0.015
60	0.11	0.05	0.007
70	0.09	0.03	0.005
80	0.075	0.02	0.0035
90	0.06	0.01	0.0035
100	0.04	0.006	0.004
110	0.03	0.007	0.006
120	0.03	0.015	0.008
130	0.04	0.025	0.011
140	0.055	0.04	0.013
150	0.07	0.055	0.016
160	0.08	0.07	0.017
170	0.09	0.08	0.018
180	0.1	0.085	0.019
ICS[a] (expt)	5.4 ± 1.6	3.7 ± 1.1	1.0 ± 0.3
ICS (VD[b])	3.06 ± 1.10	3.53 ± 0.85	1.69 ± 0.34
ICS (thry)	3.25	3.07	2.45

[a] ICS in units of 10^{-18} cm^2.
[b] Vaughan and Doering (1988).

Uncertainty in the determination of ICS values was a culmination of all the errors associated with the DCS determinations, in addition to the inherent uncertainty in extrapolating across the unmeasured angular range. Since the DCSs in the extrapolated region are small compared to those within the measured region (three to four orders of magnitude down from 0°), the extrapolation details have only a small effect on the ICS determination. By adjusting the extrapolations and examining resultant ICS values, we found a worst case variation of the order of 10%. This is consistent with the fact that, at angles larger than 25°, the extrapolated contribution to the ICS is, on average, about 16% at the present impact energies. Combining the extrapolation uncertainty with the errors previously assigned to the DCS measurements, we arrived at ICS error estimates of 29% at 30 and 50 eV, and 25% at 100 eV.

6. Discussion

In general, the measured DCSs show reasonable agreement with the measurements of Vaughan and Doering (1987, 1988). Excellent agreement is seen for the 130.4 nm line at all measured energies. The 102.7 nm feature shows good agreement at 50 eV while the current values are larger than Vaughan and Doering's at 30 eV and smaller at 100 eV. The data for the 98.9 nm feature show very good agreement at 30 eV. At 50 and 100 eV, we still see good relative

Table 5. $2s^2 2p^4\ ^3P \to 3s'\ ^3D$ (98.9 nm, $\Delta E_0 = 12.53$ eV).

	DCS ($\times 10^{-18}$ cm^2 sr^{-1})		
θ (deg)	$E_0 = 30$ eV	$E_0 = 50$ eV	$E_0 = 100$ eV
0	14.60 ± 3.94	29.23 ± 7.89	37.98 ± 8.74
5	13.26 ± 3.58	20.72 ± 5.60	12.91 ± 2.97
10	11.14 ± 3.01	7.90 ± 2.13	3.63 ± 0.83
15	6.18 ± 1.67	2.39 ± 0.65	0.89 ± 0.20
20	3.01 ± 0.81	0.72 ± 0.20	0.26 ± 0.06
25	1.12 ± 0.30	0.37 ± 0.10	0.06 ± 0.01
30	0.6	0.25	0.03
40	0.3	0.1	0.015
50	0.2	0.07	0.01
60	0.15	0.05	0.008
70	0.14	0.038	0.006
80	0.135	0.03	0.005
90	0.13	0.024	0.005
100	0.12	0.012	0.006
110	0.1	0.008	0.009
120	0.08	0.015	0.012
130	0.09	0.05	0.02
140	0.12	0.1	0.03
150	0.17	0.16	0.045
160	0.23	0.21	0.05
170	0.28	0.26	0.065
180	0.3	0.28	0.07
ICS[a] (expt)	5.3 ± 1.5	3.1 ± 0.9	1.5 ± 0.4
ICS (VD[b])	5.07 ± 1.9	5.87 ± 1.4	4.48 ± 0.9
ICS (thry)	6.50	5.79	4.54

[a] ICS in units of 10^{-18} cm^2.
[b] Vaughan and Doering (1987).

agreement but the DCSs differ in absolute terms. At 30 eV, the measured 87.8 nm DCSs agree within experimental uncertainties while a discrepancy develops in the higher angles of the 50 and 100 eV data sets where the present data suggest a slightly steeper drop off of the DCSs with increasing scattering angle.

The *R*-matrix theory, in general, does a reasonable job of predicting the shape of the DCSs within the measured angular range at the impact energies under investigation. The theory is also relatively successful at predicting the magnitude of the DCSs. However, the theoretical values tend to be slightly larger than the present experimental data.

Present ICSs show agreement with those reported by Vaughan and Doering (1987, 1988) within the quoted error limits for all measured transitions and impact energies with the exceptions of the 102.7 nm ICS at 100 eV and the 98.9 nm ICSs at 50 and 100 eV. Of particular note is the excellent agreement seen in the 130.4 nm data at all three energies investigated in this paper.

The ICS values calculated in the present *R*-matrix theory show some agreement with their experimentally determined counterparts. Taking the experimental uncertainties into account, approximately half of the *R*-matrix ICS values are in agreement with the experimental data, while the other half generally overestimate the cross sections.

The agreement between the present results and the Vaughan and Doering (1987, 1988) data is particularly significant given the differences in how the data were normalized. At 100 eV,

Table 6. $2s^2 2p^4\ ^3P \to 3s''\ ^3P$ (87.8 nm, $\Delta E_0 = 14.11$ eV).

θ (deg)	DCS ($\times 10^{-18}$ cm^2 sr^{-1})		
	$E_0 = 30$ eV	$E_0 = 50$ eV	$E_0 = 100$ eV
0	14.67 ± 3.96	59.97 ± 16.19	165.29 ± 38.02
5	12.77 ± 3.45	38.25 ± 10.33	58.54 ± 13.47
10	11.52 ± 3.11	18.41 ± 4.97	13.97 ± 3.21
15	7.40 ± 2.00	7.26 ± 1.96	3.09 ± 0.71
20	3.43 ± 0.93	2.60 ± 0.70	1.63 ± 0.37
25	2.03 ± 0.55	1.07 ± 0.29	0.31 ± 0.07
30	1	0.5	0.12
40	0.35	0.15	0.05
50	0.21	0.1	0.03
60	0.16	0.08	0.016
70	0.145	0.06	0.008
80	0.12	0.05	0.006
90	0.11	0.04	0.0055
100	0.1	0.035	0.0065
110	0.09	0.035	0.01
120	0.09	0.045	0.017
130	0.1	0.07	0.03
140	0.11	0.1	0.045
150	0.13	0.14	0.065
160	0.15	0.17	0.08
170	0.16	0.19	0.09
180	0.17	0.2	0.095
ICS[a] (expt)	5.9 ± 1.7	6.6 ± 1.9	5.8 ± 1.5
ICS (VD[b])	6.77 ± 2.4	10.92 ± 2.5	7.40 ± 1.5
ICS (thry)	5.48	5.90	4.88

[a] ICS in units of 10^{-18} cm^2.
[b] Vaughan and Doering (1988).

Vaughan and Doering's 130.4 nm data were normalized using the DCS of a He reference gas. The relative abundances of O and He were determined using the relationship between the forward scattering DCS and the optical oscillator strength (OOS) given by Celotta and Huebner (1979) (see Doering and Vaughan (1986)). This required use of OOS standards for two features; one in O and one in the reference gas. He was also used as a reference gas at 50 eV while Ar was used at 30 eV. However, the OOS method is invalid at these lower energies (i.e. must be in the Born region), and, therefore, experiments were performed at 100 eV to determine the relative abundances using the OOS method. Further explanation of the low-energy abundance ratio determinations can be found in Vaughan and Doering (1986). Computer fittings of the 130.4 nm data were then performed to give the 'best' DCS values (Vaughan and Doering 1987). Having determined absolute DCSs for the 130.4 transition, these were used as normalization standards for the other measured transitions (Vaughan and Doering 1988).

In contrast, the present DCSs were all normalized directly to measured O_2 DCS values (Johnson and Kanik 2001) on a point by point basis. Furthermore, the current DCSs were normalized based on directly measured number density ratios of O to O_2.

Given the differences in approach and the level of agreement between the present values and those of Vaughan and Doering (1987), we feel that the DCS and ICS values for the 130.4 nm
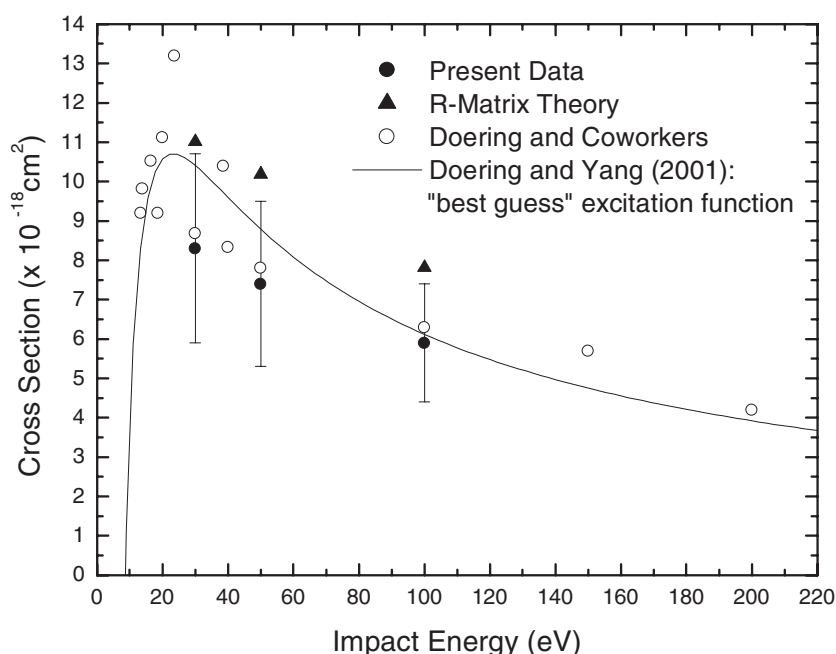
Figure 6. Present ICS values are plotted alongside the accumulated results of Doering and co-workers ((40 eV) Vaughan and Doering (1986), (30, 50, 100, 150, 200 eV) Vaughan and Doering (1987), (13.87, 16.5, 20 eV) Gulcicek and Doering (1988), (13.4, 18.6, 23.6, 38.6 eV) Doering and Yang (2001)) for the $2s^2 2p^4$ $^3P \rightarrow 3s$ ^3S transition (130.4 nm). Included in the figure is the 'best guess' for the O I (130.4 nm) feature excitation function given by Doering and Yang (2001). The reader is referred to the above referenced papers for the uncertainties in the data of Doering and co-workers. Present R-matrix results have also been included for comparison.

transitions can be considered well established at 30, 50, and 100 eV impact energies.

A useful comparison can also be made with recent atomic O emission studies. However, this discussion is left for the companion paper (Noren *et al* (2001), to be found directly following the current paper) where electron-impact-induced emission cross sections for the O I (130.4 nm) feature are presented.

Figure 6 shows a summary of the 130.4 nm ICS results of Doering and co-workers (Vaughan and Doering 1986, 1987, Gulcicek and Doering 1988, Doering and Yang 2001) in the 0–200 eV impact energy range along with the present results. The solid line in the figure is the analytical function given by Doering and Yang (2001) to represent the 'best guess' for the excitation function of the O I (130.4 nm) feature from threshold to 200 eV impact energy. This best guess was obtained by fitting a 'Bethe line' to a plot of collision strength (ICS $\times E_0$) versus $\log(E_0)$ using all of the ICS results published by Doering and co-workers (Vaughan and Doering 1987, Gulcicek and Doering 1988, Doering and Yang 2001), with the exception of the 40 eV value of Vaughan and Doering (1986). The ICSs were obtained by integrating the corresponding DCSs for each energy. As discussed, this process involves extrapolation of the measured DCS values to experimentally inaccessible angles.

In order to accurately interpret the data presented in figure 6, one must keep a couple of points in mind. First of all, examination of the published DCS results from which the ICS values in figure 6 were derived reveals that the Doering data can be separated into two groups based on whether or not low-angle DCSs were measured or extrapolated. In the case of the 30,

40, 50, 100, 150, and 200 eV data (Vaughan and Doering 1986, 1987), DCSs were measured over a range of scattering angles starting from 5°. In contrast, the DCSs leading to the ICS values at 13.4, 13.87, 16.5, 18.6, 20, 23.6, and 38.6 eV (Gulcicek and Doering 1988, Doering and Yang 2001), presumably due to large background signals at small angles and low energies, were not measured below 15°, with the exception of the 18.6 eV data where a 10° DCS value was reported. The absence of low-angle measurements in the latter group is significant due to the highly forward peaked nature of the O I (130.4 nm) DCS. This results in a substantial amount of the total ICS being generated by the extrapolation down to 0° scattering angle. A simple integration of the DCS data indicates that the extrapolated low-angle contribution reached as high as 68% of the total ICS reported at 38.6 eV. Although this effect diminishes with decreasing impact energy, due to the observed 'flattening' of the DCSs, the contribution of the extrapolated low-angle regions (0–15°) to the reported ICSs was still about 20% at 13.4 eV and already of the order of 31% at 16.5 eV.

The second point that should be made is regarding the 'best guess' of the 130.4 nm excitation function put forth by Doering and Yang (2001). As mentioned earlier, this 'guess' was obtained by fitting a Bethe line over the entire energy range of experimental ICS data presented by the paper in question. However, the functional form of the Bethe line is obtained within the Bethe–Born approximation, and is, as stated in the literature (Heddle and Gallagher 1989, Inokuti 1971, Shemansky *et al* 1985a, b, Kanik *et al* 1995, and references therein), only valid at high-impact energies (i.e. $E_0 \gg E_{th}$; where E_{th} is the transition threshold energy).

The Bethe line yields a straight line on a plot of collision strength versus the logarithm of the impact energy (i.e. a Bethe plot) with slope that is, as pointed out by Doering and Yang (2001), related to the OOS and intercept related to E_{th}. However, the Bethe line obtained by Doering and Yang (2001) yields an OOS value of 0.036 which is 25% lower than the well established value of 0.048 (Doering *et al* 1985b). In contrast, if one fits the Bethe line to the Vaughan and Doering (1987) values at 100, 150, and 200 eV, where the Bethe–Born approximation is valid, one arrives at the correct OOS to within 3% while generating a significantly different shape function than that reported by Doering and Yang (2001). Although one might argue that using the Bethe line down to the threshold is acceptable if one does not attempt to extract a physical meaning from the fitting parameters and allow them to assume unphysical values, we feel that a linear fit is simply too restrictive for this argument to hold. By forcing a linear shape to the Bethe plot over all impact energies, one is inherently coercing the physics of high energy into an inappropriate kinematic regime. We, therefore, feel that the employment of the Bethe line in this context is inappropriate and its implications can be misleading. In order to accurately describe the entire energy region, one must use additional parameters in the fitting function as described by Shemansky *et al* (1985a, b).

7. Conclusions

We have measured and reported absolute DCSs for the $2s^2 2p^4 \, ^3P \rightarrow 3s \, ^3S$ (130.4 nm), $2s^2 2p^4 \, ^3P \rightarrow 3d \, ^3D$ (102.7 nm), $2s^2 2p^4 \, ^3P \rightarrow 3s' \, ^3D$ (98.9 nm) and $2s^2 2p^4 \, ^3P \rightarrow 3s'' \, ^3P$ (87.8 nm) transitions at 30, 50, and 100 eV electron-impact energies. DCSs were measured between scattering angles of 0° and 25° (0° and 20° in the 12.07 nm, $E_0 = 100$ eV case). The DCSs were then extrapolated to 180° and integrated over all angles to produce ICSs. Comparison was made between the present results and those of Vaughan and Doering (1987, 1988) showing reasonable agreement with both the DCSs and ICSs. Theoretical *R*-matrix predictions were presented and gave a reasonable representation of the shape and magnitude of the DCSs but gave significantly overestimated ICS values in some cases.

Due to the good agreement between the 130.4 nm DCS and ICS data of this paper and

that of Vaughan and Doering (1987), we conclude that the cross sections for this transition can be considered well established at 30, 50, and 100 eV.

Presently, there is an absence of small angle DCS measurements at low energies for the O I (130.4 nm) line in the literature which calls into question the reliability of the corresponding ICSs which are available at present. This suggests that further DCS and ICS measurements are needed in this regime (<30 eV) in order to firmly establish the low-energy behaviour. To this end, the current authors are extending the range of measurements into the lower-energy region by making use of a novel electron time-of-flight normalization technique pioneered by LeClair *et al* (1996). Results are expected to be available in the near future.

Acknowledgments

Appendix. Determination of the ratio of O to O_2 number densities

Let $R(O_2)_{in}$ be the flow rate of O_2 into the discharge source. If we assume that the only dissociation products are neutral O atoms, then, after leaving the discharge source, O and O_2 are found in the following proportions:

$$D(O + O) : (1 - D)O_2. \tag{A.1}$$

Therefore, the flow rates of O and O_2 out of the source can be written in terms of $R(O_2)_{in}$ as

$$R(O)_{out} = 2DR(O_2)_{in} \tag{A.2}$$

$$R(O_2)_{out} = (1 - D)R(O_2)_{in}. \tag{A.3}$$

Alternatively, we can write the outgoing flow rates in terms of the number densities, n^{on}_{O/O_2}, and mean velocities, v_{O/O_2}, of O and O_2 exiting the discharge source, i.e.

$$R(O)_{out} = An^{on}_O v_O \tag{A.4}$$

$$R(O_2)_{out} = An^{on}_{O_2} v_{O_2} \tag{A.5}$$

where A is the cross sectional area of the discharge tube. Combining equations (A.2)–(A.5), one arrives at the following expression:

$$\frac{n^{on}_O}{n^{on}_{O_2}} = \frac{2D}{(1 - D)} \frac{v_{O_2}}{v_O}. \tag{A.6}$$

If one assumes thermal equilibrium along with Boltzmann velocity distributions for the beam constituents, then the ratio of the O_2 to O mean velocities can be written in terms of their masses, m_{O/O_2}, as

$$\frac{v_{O_2}}{v_O} = \sqrt{\frac{m_O}{m_{O_2}}}. \tag{A.7}$$

Substituting (A.7) into equation (A.6) one gets

$$\frac{n^{on}_O}{n^{on}_{O_2}} = \frac{\sqrt{2}D}{(1 - D)} \tag{A.8}$$

where we have made use of the fact that $m_{O_2} = 2m_O$.

References

Ajello J M, James G K, Franklin B O and Shemansky D E 1989 *Phys. Rev.* A **40** 3524

Athay R G and Judge P G 1995 *Astrophys. J.* **438** 491

Berrington K A, Eissner W B and Norrington P H 1995 *Comput. Phys. Commun.* **92** 290

Celotta R J and Huebner R 1979 *Electron Spectroscopy: Theory, Techniques, and Applications* ed C Brundle and A Baker (Orlando, FL: Academic) p 41

Clementi E and Roetti C 1974 *At. Data Nucl. Data* **14** 177

Doering J P 1992 *Geophys. Res. Lett.* **19** 449

Doering J P and Gulcicek E E 1989a *J. Geophys. Res.* **94** 1541

——1989b *J. Geophys. Res.* **94** 2733

Doering J P, Gulcicek E E and Vaughan S O 1985a *Chem. Phys. Lett.* **114** 334

——1985b *J. Geophys. Res.* **90** 5279

Doering J P and Vaughan S O 1986 *J. Geophys. Res.* **91** 3279

Doering J P and Yang J 2001 *J. Geophys. Res.* **106** 203

Erdman P W and Zipf E C 1987 *J. Chem. Phys.* **87** 3381

Gulcicek E E and Doering J P 1987 *J. Geophys. Res.* **92** 3445

——1988 *J. Geophys. Res.* **93** 5879

Gulcicek E E, Doering J P and Vaughan S O 1988 *J. Geophys. Res.* **93** 5885

Heddle D W O and Gallagher J W 1989 *Rev. Mod. Phys.* **61** 221

Hibbert A 1975 *Comput. Phys. Commun.* **9** 141

Inokuti M 1971 *Rev. Mod. Phys.* **43** 297

Itikawa Y and Ichimura A 1990 *J. Phys. Chem. Ref. Data* **19** 637

James G K, Ajello J M, Franklin B and Shemansky D E 1990 *J. Phys. B: At. Mol. Opt. Phys.* **23** 2055

Johnson P V and Kanik I 2001 *J. Phys. B: At. Mol. Opt. Phys.* submitted

Julienne P S and Davis J 1976 *J. Geophys. Res.* **81** 1397

Kanik I, Beegle L W, Ajello J M and Solomon S C 2000 *Phys. Chem. Earth* **25** 573

Kanik I, James G K and Ajello J M 1995 *Phys. Rev.* A **51** 2067

LeClair L R, Trajmar S, Khakoo M A and Nickel J C 1996 *Rev. Sci. Instrum.* **67** 1753

Murphy E J and Brophy J H 1979 *Rev. Sci. Instrum.* **50** 635

Noren C, Kanik I, Johnson P V, McCartney P, James G K and Ajello J M 2001 *J. Phys. B: At. Mol. Opt. Phys.* **34** 2667

Rountree S P 1977 *J. Phys. B: At. Mol. Phys.* **10** 2719

Rountree S P and Henry R J W 1972 *Phys. Rev.* A **6** 2106

Shemansky D E, Ajello J M and Hall D T 1985a *Astrophys. J.* **296** 765

Shemansky D E, Ajello J M, Hall D T and Franklin B 1985b *Astrophys. J.* **296** 774

Shyn T W, Cho S Y and Sharp W E 1986 *J. Geophys. Res.* **91** 13751

Shyn T W and Sharp W E 1986 *J. Geophys. Res.* **91** 1691

Smith E R 1976 *Phys. Rev.* A **13** 65

Stone E J and Zipf E C 1974 *J. Chem. Phys.* **60** 4237

Tayal S S and Henry R J W 1988 *Phys. Rev.* A **38** 5945

——1989 *Phys. Rev.* A **39** 4531

——1990 *Phys. Rev.* A **42** 320

Trajmar S and Kanik I 1995 *Atomic and Molecular Processes in Fusion Edge Plasmas* ed R K Janev (New York: Plenum) pp 31–58

Trajmar S and Register D F 1984 *Electron Molecule Collisions* ed K Takayanagi and I Shimamura (New York: Plenum) pp 427–93

Vaughan S O and Doering J P 1986 *J. Geophys. Res.* **91** 13755

——1987 *J. Geophys. Res.* **92** 7749

——1988 *J. Geophys. Res.* **93** 289

Wang S and McConkey J W 1992 *J. Phys. B: At. Mol. Opt. Phys.* **25** 5461

Zecca A, Karwasz G P and Brusa R S 1996 *Nuovo Cimento* **19** 1

Zipf E C 1986 *J. Phys. B: At. Mol. Phys.* **19** 2199

Zipf E C and Erdman P W 1985 *J. Geophys. Res.* **90** 11087

Zipf E C and Kao W W 1983 *EOS Trans. Am. Geophys. Union* **64** 785

——1986 *Chem. Phys. Lett.* **125** 394

Zipf E C, Melaughlin R W and Gorman M R 1979 *Planet. Space Sci.* **27** 719